RESEARCH PROPOSAL

Image-space wave-equation tomography for quality factor Q

Yi Shen

2:30 P.M., Wednesday, November 28th, 2012

ABSTRACT

Quantitative estimates of quality factor Q are useful for a variety of applications, ranging from seismic-acquisition design, to seismic processing, amplitude analysis, and reservoir characterization. However, Q model building, which is conventionally done in the data space using ray-based tomography, is a notoriously challenging problem due to issues like spectral interference, low signal-to-noise ratio, diffractions, and complex subsurface structure. I propose to produce reliable Q models using a new approach with two major features. First, this method will be performed in the image-space, which uses downward-continuation compensation migration with Q to stack out noise, focus and simplify events, and provide a direct link between the model perturbation and the image perturbation. Second, this method uses wave-equation Q tomography (WEQTom) to handle the complex wave propagation. The implementation of the compensation migration and WEQTom operator builds the cornerstone of the proposed process, and the preliminary results on a simple 2-D example demonstrate its feasibility. Finally, a synthetic test on a 2-D model with multiple reflectors and a Gaussian Q anomaly shows the capability of this method on a realistic structure with a gas cloud.

INTRODUCTION

Problem Statement

Anelastic attenuation, parametrized by seismic quality factor, Q, has considerable impacts on surface seismic reflection data. An understanding of the effects and properties of this attenuation parameter has three major motivations.

First, Q is a useful parameter for characterizing rock and fluid properties–e.g., saturation, porosity, permeability, and viscosity–because of its high sensitivity to some of these properties (e.g. Best et al. (1994)). For example, Q can serve as a lithology discriminator in a frontier area with sparse well control (Dasgupta and Clark, 1998). In addition, as the magnitude of the attenuation is directly related to petrophysical parameters, Q analysis provides a potential tool for reservoir characterization; it can help determine the contents (e.g. gas saturation) of a reservoir (Winkler and Nur, 1982), map fracture azimuth to target reservoir development (Clark et al., 2001; Maultzsch et al., 2007; Clark et al., 2009), and monitor the mobility of reservoir fluids to optimize the injection process (Macrides and Kanasewich, 1987).

Second, if the absorption properties of the subsurface are known, they can be included in seismic data processing (deconvolution, stacking, migration, inverse Q filtering, etc.) to get sharper images and higher resolution. Estimates of attenuation could also be used to better interpret the effects of AVO and anisotropy, which also have offset-dependent signatures. Furthermore, full waveform inversion can achieve improved accuracy by incorporating attenuation into the initial model.

Third, estimates of attenuation are useful in seismic acquisition design. Knowing seismic attenuation in the survey-planning stage helps predict how much signal may reach the target, and enables the optimization of acquisition parameters.

Studies estimating attenuation tomographically have a long history. Brzostowski and McMechan (1992), and Leggett et al. (1992) used the change in seismic amplitude as observed data for attenuation tomography. Kjartansson (1979), and Zucca et al. (1994) measured the rise time of the broadened wavelets caused by attenuation for Q tomography. Tonn (1991), Quan and Harris (1997), Dasgupta and Clark (1998), Leaney (1999), Mateeva (2003), Plessix (2006), Rickett (2006), Rickett (2007), Reine et al. (2012a), and Reine et al. (2012b) performed the estimation based on the attenuation-induced spectral changes. However, there are three main difficulties that cause the estimated Q model from these methods to be unreliable. First, Q tomography schemes in these works are mostly ray-based, measuring the spectral changes over different lengths of raypaths, which are prone to errors and unrealistic results when multi-pathing exists in areas of complex overburden. Second, measurements conducted in these works are all in the data domain, which has a number of issues that can affect the accuracy of Q model building. Specifically, diffractions and poor signal-to-noise ratio introduce large errors in Q estimation. In addition, the events in the data domain are crossed (Figure 1(a)), which will introduce spectral interference. Third, attenuation-free reference/source spectra are required for these Q measurements, which may be not be available in practice. Therefore, a new technique that yields reliable Q models is needed.

PROPOSED SOLUTION

I propose to produce a reliable Q model by using image-space wave-equation tomography. As mentioned in previous sections, in the presence of complex wave propagation (i.e. multipathing), ray-based methods often cannot produce high-quality images, while wavefield-continuation methods yield better images, due to their ability to handle multipathing of the reflected energy. Moreover, the data-space approach is vulnerable when the data are contaminated with noise, diffractions and crossing events; whereas the image-space approach is stable, because migration suppresses the noise and focuses the events. For example, the crossing events in the data space are separated in the image space (Figure 1(b)), avoiding spectral interference and improving the accuracy of attenuation calculations. To some degree, the migration-based technique is also more efficient than the data-based one, since it can be implemented in a target-oriented fashion and hence focus on the attenuated zone.

Therefore, I propose to design a mechanism – a wave-equation Q tomography (WEQTom) operator – that provides a direct mapping between the change in the image space and the change in the Q model. This idea is similar to wave-equation migration velocity analysis (WEMVA) (Sava and Biondi, 2004; Biondi, 2006), which relates image perturbation with velocity perturbation. The change in the image can be measured either by computing the difference between the attenuated stacked image

and the attenuation-free stacked image, or by computing the spectral variation of each event over angles in the angle-domain common-image gathers (ADCIGs). The former measurement requires the source spectrum, while the latter measurement does not, because it compares the image spectrum at a certain subsurface angles to the one at zero-subsurface angle. Finally, the back-projected changes in the Q model space will be used as gradient directions to conduct a line-search in optimization schemes.

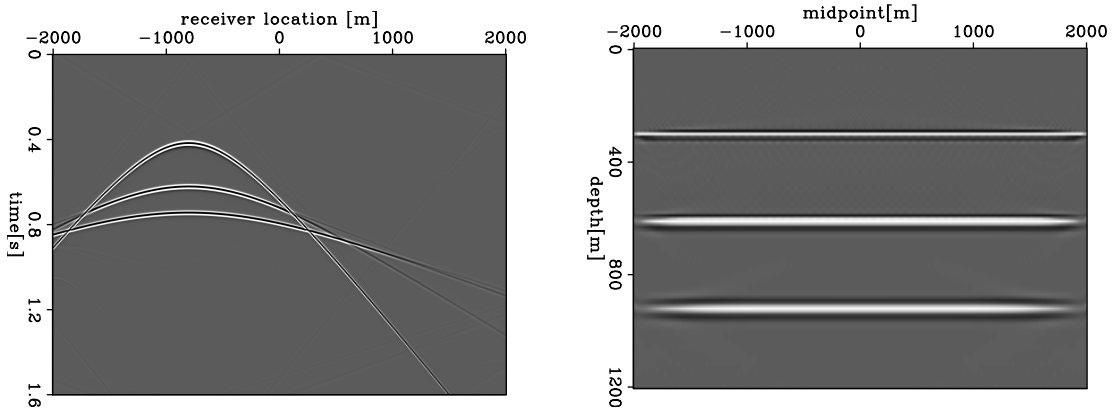

(a) (b)

Figure 1: (a) The events around t=0.8s are crossed in the prestack data domain; (b) the crossing events shown in Figure 1(a) are separated.

THEORY

Seismic wave attenuation includes intrinsic attenuation and scattering attenuation. Intrinsic attenuation transfers wave energy to heat. Scattering attenuation transfers wave energy to later arrivals or to other directions. The theory in this section concentrates on the intrinsic attenuation and tries to reduce the influence of the scattering attenuation. In the situation when the scattering attenuation cannot be ignored, the estimated attenuation is a combination of intrinsic and scattering effects.

Attenuation changes both the phase and the amplitude spectrum of a wave propagating through an absorptive medium. The phase change due to attenuation is barely measurable within the seismic frequency bandwidth. Therefore it is neglected for Q model building.

On the other hand, attenuation has a first-order effect on the amplitude spectrum. However, the amplitude of a wave not only decays exponentially due to attenuation, but also decreases due to other factors, such as geometric spreading, instrument response, source/receiver coupling, radiation patterns, and reflection/transmission effects. Among these terms, the attenuation effect is the only frequency-dependent term. Therefore, instead of working with the absolute scaling of the amplitude spectrum, I will examine the frequency-dependent amplitude change to quantify the attenuation effect.

In the following sections, I will first present downward-continuation imaging with Q to provide the basis for image-based Q tomography. Second, I will present a wave-equation Q tomography operator to relate the perturbed imaging to the Q model. Third, I will introduce the spectral ratio (Tonn, 1991) method, which will be used in the last section (Image perturbation estimation).

Downward-continuation imaging with Q

Valenciano et al. (2011) presented a one-way viscoacoustic wave-equation approach that can accurately migrate data in media with attenuation. Their approach uses an extension of the Fourier Finite-Differences(FFD) algorithm to compensate for the effects of Q during migration. Due to the relatively large frequency dispersion for FFD, I extend the explicit split-step algorithm to migrate the attenuated data.

I present both migration with Q and compensation migration with Q in the following section. Migration with Q incorporates Q in the conventional migration and implements the adjoint of the viscoacoustic modeling, which further attenuates the wavefield through imaging. Compensation migration with Q is designed to regain the energy through downward continuation, which is able to recover the amplitude and phase change due to attenuation. The image obtained by compensation migration with Q will be identical to the image without attenuation. Therefore, I will use this method in the image-based Q tomography.

I will use the nearly constant-Q (frequency independent) model (Futterman, 1962) for both migration and compensation migration. This assumption is supported by physical experiments which show that Q is nearly constant within the seismic frequency range.

Downward-continuation migration with Q

In a linear attenuating medium, the one-way wave equation used for migration by wavefield continuation has the following phase-shift recursive solution:

$$P_{z+\Delta z}\left(\omega, k_x, k_y\right) = P_z\left(\omega, k_x, k_y\right) e^{\pm i k_z \Delta z}. \tag{1}$$

where P is the pressure, ω is the temporal frequency, k_x and k_y are the horizontal wavenumbers, and k_z is the vertical wavenumber. The plus and minus signs in the phase shift operator represent downgoing and upgoing waves, respectively.

The vertical wavenumber can be expressed by the following dispersion relation, which is often called the Single Square Root (SSR) equation:

$$\begin{aligned} k_z &= \mathrm{SSR}(\omega, \mathbf{k}) \\ &= \sqrt{(\omega \tilde{s})^2 - |\mathbf{k}|^2} \end{aligned} \tag{2}$$

where $|\mathbf{k}| = \sqrt{k_x^2 + k_y^2}$; $\tilde{s}$ is the phase slowness, which becomes a complex number and can be given by following equation based on the nearly constant-Q model (Futterman, 1962),

$$\tilde{s}(\omega) = s_{\omega r}\left(1 - \frac{1}{\pi Q}\ln(\omega/\omega_r)\right)\left(1 + \frac{i}{2Q}\right), \tag{3}$$

where $s_{\omega r}$ is the slowness at a reference frequency ω_r. Since attenuation delays more at the lower frequencies than the higher frequencies, I will take the infinite frequency as the reference frequency (the Nyquist frequency in the real case).

The phase-shift migration operator described above is strictly valid for a subsurface model that varies only with depth. To extend the operator to handle laterally varying earth models, a simplified form of this SSR can be approximated by using Taylor expansion around the reference slowness $\tilde{s}_0$ and the reference quality factor Q_0:

$$k_z(s_{\omega r}, Q) = k_{z0}(\tilde{s}_0) + \omega\,(\tilde{s} - \tilde{s}_0), \tag{4}$$

where

$$\tilde{s}_0 = s_{\omega r0}\left(1 - \frac{1}{\pi Q_0}\ln(\omega/\omega_r)\right)\left(1 + \frac{i}{2Q_0}\right). \tag{5}$$

Equation 4 describes split-step migration, whose accuracy can be improved by using more than one reference slowness and Q. In this modified scheme, often called Extended Split-Step migration, multiple reference wavefields are generated. A single wavefield is then estimated at each depth step by an interpolation in the space domain. At each spatial location, the interpolation weights are computed according to the difference between the actual medium slowness/Q and the respective reference slowness/Q.

Downward-continuation compensation migration with Q

The vertical wavenumber shown in Equation 2 becomes a complex number with attenuation being included in its imaginary part to reduce the amplitude, and in its real part to change the phase. Q migration recovers the phase change, since it flips the sign of the phase term during downward continuation migration. However, the sign of the amplitude term remains unchanged in this extrapolation, which further reduces the amplitude of the attenuated data. In order to compensate for the amplitude loss, Equation 1 needs to be rewritten into the following form to regain the amplitude (imaginary part):

$$P_{z+\Delta z}\left(\omega, k_x, k_y\right) = P_z\left(\omega, k_x, k_y\right)\frac{\exp\left(\pm i k_z\right)}{\exp\left(\pm 2i\left(\mathrm{Im}\left(k_z\right) - \mathrm{Im}\left(k_{\mathrm{NQ}}\right)\right)\right)}, \tag{6}$$

where k_{NQ} is the vertical wavenumber without attenuation, and can be expressed in the following way,

$$k_{\mathrm{NQ}} = \sqrt{(\omega s_{wr})^2 - |\mathbf{k}|^2}. \tag{7}$$

The denominator in Equation 6 compensates for the amplitude loss due to attenuation.

Wave-equation Q tomography operator

I present the image-space WEQTom operator in this section; its process is similar to WEMVA (Sava and Biondi, 2004; Biondi, 2006). WEQTom is a non-linear inversion process that aims to find the Q model that minimizes the residual field in the image space. In general, the residual image, $\Delta\mathbf{I}$, is the difference between the background image, $\mathbf{I}$, computed with the current background model and the 'target' image, which will be fully discussed in the later section. In the least-squares sense, the tomographic objective function can be written as follows:

$$J = \frac{1}{2}||\Delta\mathbf{I}||_2. \tag{8}$$

In this paper, I evaluate the wave-equation tomographic operator in the shot-profile domain. Both source and receiver wavefields are downward continued in the shot-profile domain using the one-way wave equations (Claerbout, 1971):

$$\begin{cases} \left(\frac{\partial}{\partial z} + ik_z\right) D(\mathbf{x}, \mathbf{x}_s) = 0 \\ D(x, y, z = 0, \mathbf{x}_s) = f_s\delta(\mathbf{x} - \mathbf{x}_s) \end{cases}, \tag{9}$$

and

$$\begin{cases} \left(\frac{\partial}{\partial z} - ik_z\right) U(\mathbf{x}, \mathbf{x}_s) = 0 \\ U(x, y, z = 0, \mathbf{x}_s) = P(x, y, z = 0, \mathbf{x}_s) \end{cases}, \tag{10}$$

where $D(\mathbf{x}, \mathbf{x}_s)$ is the source wavefield at the image point $\mathbf{x} = (x, y, z)$ with the source located at $\mathbf{x}_s = (x_s, y_s, 0)$; $U(\mathbf{x}, \mathbf{x}_s)$ is the receiver wavefield at the image point $\mathbf{x}$ with the source located at $\mathbf{x}_s$; f_s is the source signature, and $f_s\delta(\mathbf{x} - \mathbf{x}_s)$ defines the point source function at $\mathbf{x_s}$, which serves as the boundary condition of equation 9; $P(x, y, z = 0, \mathbf{x}_s)$ is the recorded shot gather at $\mathbf{x}_s$, which serves as the boundary condition of Equation 10; and k_z is the same vertical wavenumber as shown in Equation 2.

The background image is computed by applying the cross-correlation imaging condition:

$$I(\mathbf{x}, \mathbf{h}) = \sum_{\mathbf{x}_s}\sum_{\omega} \overline{D(\mathbf{x} - \mathbf{h}, \mathbf{x}_s)}U(\mathbf{x} + \mathbf{h}, \mathbf{x}_s), \tag{11}$$

where the bar stands for the complex conjugate, and $\mathbf{h} = (h_x, h_y, h_z)$ is the subsurface half-offset.

Under the Born approximation, a perturbation in the model parameters causes a first-order perturbation in the wavefields. Consequently, the resulting image perturbation reads:

$$\begin{aligned} \Delta I(\mathbf{x}, \mathbf{h}) \;=\; & \sum_{\mathbf{x}_s}\sum_{\omega} \Big(\overline{\Delta D(\mathbf{x} - \mathbf{h}, \mathbf{x}_s)}\widehat{U}(\mathbf{x} + \mathbf{h}, \mathbf{x}_s) + \\ & \overline{\widehat{D}(\mathbf{x} - \mathbf{h}, \mathbf{x}_s)}\Delta U(\mathbf{x} + \mathbf{h}, \mathbf{x}_s)\Big), \end{aligned} \tag{12}$$

where $\widehat{D}(\mathbf{x}-\mathbf{h},\mathbf{x}_s)$ and $\widehat{U}(\mathbf{x}+\mathbf{h},\mathbf{x}_s)$ are the background source and receiver wavefields computed with the background model $\widehat{Q}(\mathbf{x})$, and $\Delta D(\mathbf{x}-\mathbf{h},\mathbf{x}_s)$ and $\Delta U(\mathbf{x}+\mathbf{h},\mathbf{x}_s)$ are the perturbed source wavefield and perturbed receiver wavefield, respectively, which result from the model perturbation $\Delta Q(\mathbf{x})$.

To evaluate the adjoint tomographic operator $\mathbf{T}^*$, which backprojects the image perturbation into the model space, I first compute the wavefield perturbation from the image perturbation using the adjoint imaging condition:

$$\begin{aligned} \Delta D(\mathbf{x},\mathbf{x}_s) &= \sum_{\mathbf{h}} \Delta I(\mathbf{x},\mathbf{h})\widehat{U}(\mathbf{x}+\mathbf{h},\mathbf{x}_s) \\ \Delta U(\mathbf{x},\mathbf{x}_s) &= \sum_{\mathbf{h}} \Delta I(\mathbf{x},\mathbf{h})\widehat{D}(\mathbf{x}-\mathbf{h},\mathbf{x}_s). \end{aligned} \tag{13}$$

The perturbed source and receiver wavefields satisfy the following one-way wave equations, linearized with respect to Q:

$$\begin{cases} \left(\frac{\partial}{\partial z} + ik_z\right)\Delta D(\mathbf{x},\mathbf{x}_s) = \left(-i\frac{\partial k_z}{\partial Q}\widehat{D}(\mathbf{x},\mathbf{x}_s)\right)\Delta Q(\mathbf{x}) \\ \Delta D(x,y,z=0,\mathbf{x}_s) = 0 \end{cases}, \tag{14}$$

and

$$\begin{cases} \left(\frac{\partial}{\partial z} - ik_z\right)\Delta U(\mathbf{x},\mathbf{x}_s) = \left(-i\frac{\partial k_z}{\partial Q}\widehat{U}(\mathbf{x},\mathbf{x}_s)\right)\Delta Q(\mathbf{x}) \\ \Delta U(x,y,z=0,\mathbf{x}_s) = 0 \end{cases}, \tag{15}$$

When solving the optimization problem, I obtain the image perturbation by comparing the background image and the target image. Then the perturbed image is convolved with the background wavefields to get the perturbed wavefields (Equation 13). The scattered wavefields are computed by applying the adjoint of the one-way wave-equations 14 and 15. Finally, the perturbation $\Delta Q(\mathbf{x})$, is obtained by cross-correlating the upward-propagated scattered wavefields with the modified background wavefields,

$$\Delta Q(\mathbf{x}) = \sum_{x_s}\sum_{\omega} \overline{\Delta D}\left(-i\frac{\partial k_z}{\partial Q}\widehat{D}\right) + \overline{\Delta U}\left(-i\frac{\partial k_z}{\partial Q}\widehat{U}\right). \tag{16}$$

Spectral ratio

Tonn (1991) and Quan and Harris (1997) developed the `spectral ratio` and `frequency-shift` methods, respectively, to measure attenuation effects on the spectra. Both these methods assume that attenuation is the only frequency-dependent influence on the amplitude spectra, and they use one parameter to describe this influence (spectral slope in spectral ratio methods and central frequency shift in frequency-shift method).

In my study, I prefer the spectral ratio method over the frequency-shift method for three reasons. First, the frequency-shift method has to take the whole spectrum, which may contain noise at low or high frequencies (e.g. artifacts caused by the imaging operator), while the spectral ratio method only needs a certain range of frequencies, so I can choose a clean part of the spectrum. Second, I can also use least squares in the spectral ratio method to minimize the error due to large noise. Third, the central frequency is dependent not only on attenuation, but also on the type of source spectrum (e.g. Gaussian, boxcar, triangular, etc). Now I will discuss the spectral ratio method.

Assuming the amplitude spectrum of an incident wave is $S(f)$, and the response of the attenuating medium is $GH(f)$, I can write the amplitude spectrum of the outgoing wave $R(f)$ as

$$R(f) = GH(f)S(f), \tag{17}$$

where the factor G includes geometrical spreading, instrument response, source/receiver coupling, radiation pattern, and reflection/transmission coefficients, and $H(f)$ describes the attenuation effect on the amplitude. Experiments indicate that attenuation is usually proportional to frequency, that is, the response $H(f)$ may be expressed (Ward and Toksoz, 1971) as

$$H(f) = \exp\left(-f \int_{\text{ray}} \frac{\pi}{Qv}\right), \tag{18}$$

where v is wave velocity.

The medium response $H(f)$ can be estimated from the knowledge of the input spectrum $S(f)$ and the output spectrum $R(f)$. In fact, $S(f)$ does not have to be the source spectrum, but can be any spectrum extracted from the non-attenuated zone (e.g., the water bottom reflection). The relationship between the spectral ratio of $S(f)$ to $R(f)$ and the frequency is linear, as shown by the following equation,

$$Y(f) = Cf + A, \tag{19}$$

where

$$Y(f) = \ln\left[S(f)/R(f)\right], \tag{20}$$

$$C = \left(-f \int_{\text{ray}} \frac{\pi}{Qv}\right), \tag{21}$$

$$A = -\ln(G), \tag{22}$$

It can be seen that the integrated term C is the slope of the line $Y(f)$, which can be used to invert for Q. Note that the absolute scaling of these two waveforms comes out in the intercept term A. Therefore, this method automatically removes the effect of the frequency-independent factor G.

Image perturbation estimation

The goal of this tomography method is to maximize the quality of the migrated image (i.e. minimize the residual image, $\Delta\mathbf{I}$) by iteratively updating the Q model. In this section, I develop ways of measuring the image perturbation in two image domains: the stacked image domain and the subsurface angle domain. As discussed previously, the perturbed image can be measured from the perturbed amplitude spectral change after the absolute scaling of the waveform has been removed. Therefore, the residual image can be written in the following general form:

$$\Delta\mathbf{I} = \mathbf{S}^* \left(\mathbf{SMI} - \mathbf{AS}\widehat{\mathbf{I}} \right), \tag{23}$$

where $\mathbf{I}$ is the background image computed with the current background model, and $\Delta\mathbf{I}$ is the residual image. Minimizing this residual image drives the background image toward a target image $\widehat{\mathbf{I}}$ that will be discussed in the later part of this section. Operator $\mathbf{S}$ calculates the spectrum of each event in the image, and operator $\mathbf{S}^*$ transforms the spectrum back to the image space. For the synthetic model with sparse reflectors, we can easily isolate each event for spectral calculation. However, for some real cases, events can be very close to each other, so that they will be difficult to individually separate. This will introduce spectral interference to degrade the accuracy of the estimates. $\mathbf{A}$ is the scaling operator calculated by the `spectral ratio` method, which removes the frequency-independent amplitude effects. To reduce the ambiguity between weak events and noise, the masking operator $\mathbf{M}$ chooses the preferred events with strong energy for model updating. The remigration with this updated Q amplifies the energy of strongly attenuated events that can then be chosen for the following iterations.

The choice of the target image $\widehat{\mathbf{I}}$ is the main distinguishing element between the different measurements of the perturbed image. Both of these methods require accurate velocity models. Fortunately, since both velocity and Q model building share the same tomography kernel, we can updated these two models simultaneously. The following subsections describe these approaches in two different image domains and compare their effectiveness and limitations.

Stacked image domain

Estimating the perturbed image in this domain assumes that the source wavelet is well known and the reflectivity is white. The target image $\widehat{\mathbf{I}}$ is the image of a non-attenuated dataset generated by a set of picked reflectivities. The following workflow illustrates the details of this method

- **Pick reflectors**

  I design an automatic picker to pick each individual event for spectrum analysis and target image generation. The picker automatically pinpoints the local maximum of the envelope of each trace and places a normalized reflectivity R

on the reflector. During this procedure, thresholding helps choose the reflector with relatively high amplitude.

- **Generate target image $\widehat{\mathbf{I}}$**

  I synthesize a set of non-attenuated data by injecting the known source wavelet into a non-attenuated medium with reflectivity R. This data is then remigrated to obtain the non-attenuated target image $\widehat{\mathbf{I}}$.

- **Assign masks M to the background image I**

  Only key reflectors are selected to generate the target image $\widehat{\mathbf{I}}$. Therefore, an image mask $\mathbf{M}$ is needed to select the corresponding reflections in background image $\mathbf{I}$. I design the mask function $\mathbf{M}$ according to the energy of the target image $\widehat{\mathbf{I}}$.

- **Calculate the residual image ΔI**

  The residual image can be calculated using Equation 23.

This residual image $\Delta\mathbf{I}$ is less prone to spectral modification by migration, such as stacking, illumination, etc., because both the background image $\mathbf{I}$ and the target image $\widehat{\mathbf{I}}$ are the results of the same imaging operator. Furthermore, computing the perturbation requires less computational time and memory in the stacked-image domain than in the prestack domain. Therefore, this method will be used for the following synthetic tests.

Subsurface angle domain

In this measurement, the target image $\widehat{\mathbf{I}}$ is the image extracted from the zero angle. Based on the assumption that the amplitude spectra contain the same frequency contents over different angles if the Q model for compensation migration is accurate, this method minimizes the differences between the spectra of the contiguous angles in the compensated image.

Performing the measurement in the angle gathers has certain advantages. Because it compares the spectra at different angles with that of the zero angle, this method does not require the non-attenuated reference/source information that is a prerequisite for the conventional Q estimation methods. In addition, by incorporating more information with an additional axis in the prestacked domain, this method may produce higher resolution than the stacked-domain method.

However, the operator that generates the angle gathers (e.g. slant stack) may introduce additional artifacts, which hampers the spectral analysis. Also, the angle gather contains spectral stretch related to the reflection angle and structure dipping angle. Hence prior knowledge of these angles is required for correcting the spectral stretch before calculating the perturbed image.

WORK COMPLETED

Numerical test of migration and compensation migration with Q

To test the downward continuation operator with Q, I run Q migration and compensation migration on a 2-D model. The model size is 4000 m (length) x 2500 m (depth). A horizontal reflector is at 1500 m depth, and 51 sources and 401 receivers are uniformly distributed on the surface. The medium is homogeneous with constant velocity (2000 m/s) and constant Q (50 for the model with attenuation and 99999 for the model without attenuation). A Ricker wavelet with 50 Hz central frequency is used as the source wavelet for all the following synthetic tests. The reference frequency for phase correction is set to the Nyquist frequency of the source wavelet (200 Hz).

For conveniently comparing the wavelets in Figure 2, all plots are displayed in normalized wiggles, and the maximum amplitude of those wavelets before normalization are presented in the title. Figure 2(a) shows the conventional migration of the data generated from the model without attenuation, which images the reflector at 1500m depth. Figure 2(b), Figure 2(c) and Figure 2(d) shows the conventional migration, Q migration, and Q compensation migration of the data generated from the model with attenuation, respectively. Due to the higher-frequency frequencies loss and velocity dispersion caused by attenuation, the wavelets in Figure 2(b) are stretched, amplitude-decayed and phase-rotated when compared with Figure 2(a). Figure 2(c) shows that Q migration corrects the phase change, but stretches and attenuates the wavelets even more than those in Figure 2(b). This result comfirms that Q migration can compensate for phase distortion, but further reduces, instead of regaining, the amplitude of the attenuated data. Figure 2(d) presents the result of Q compensation migration on the attenuated data, showing exactly the same result as Figure 2(a), indicating that Q compensation adequately restores both the amplitude and phase.

Numerical test of the WEQTom operator

Similar to the forward tomographic operator in WEMVA (Sava and Biondi, 2004; Biondi, 2006) that linearizes the image around the slowness (inverse of velocity), the forward WEQTom operator relates the perturbation in $1/Q$ to the image perturbation by linear approximation. This approximation may fail when the model error is large. To verify the effectiveness of this linear approximation, I compare the results generated by the linearized operator and the true image perturbation that is obtained by subtracting the background image from the true image. The size of the test 2D model is 4000 m (length) x 1200 m (depth). A horizontal reflector is at 900 m depth, and 51 sources and 401 receivers are uniformly distributed on the surface. The background medium is homogeneous with constant velocity (2000 m/s) and constant Q ($1/Q = 0.02$). Figure 5(a) and Figure 5(b) show the model perturbation with rectan-

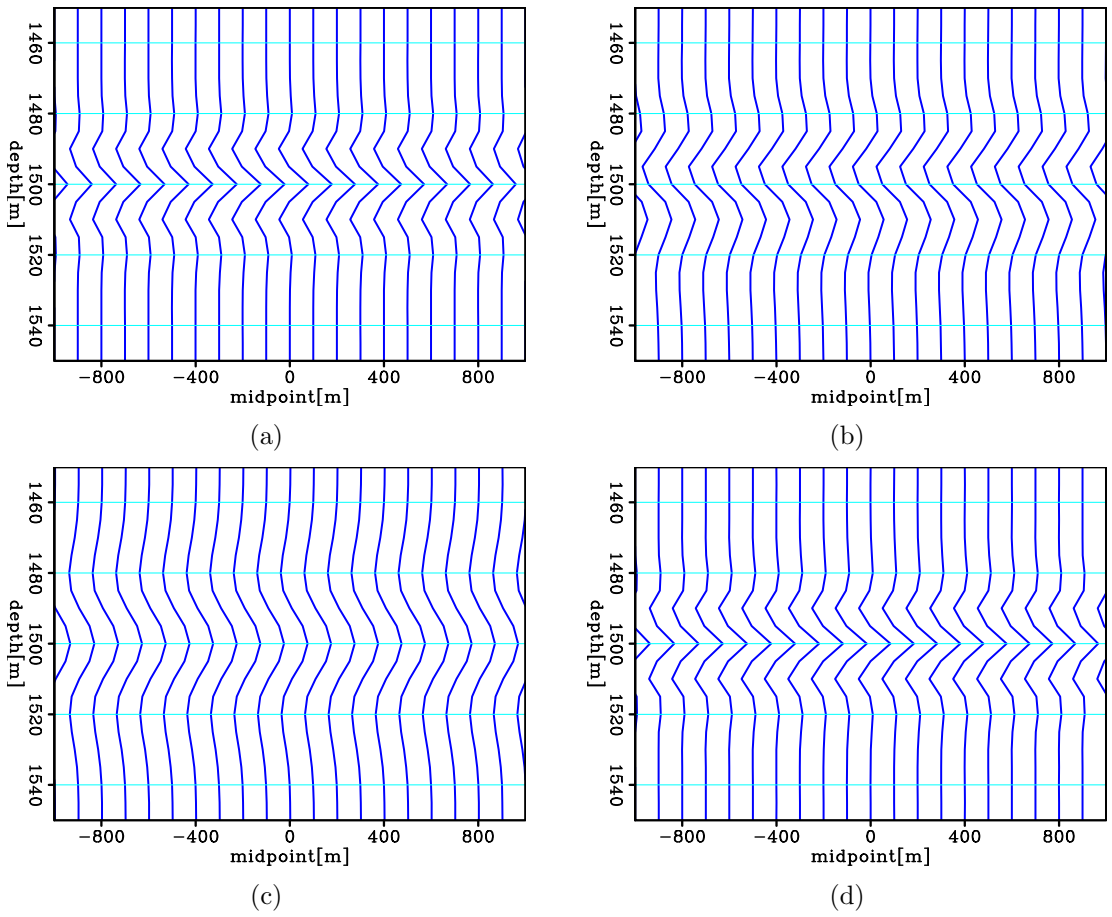

Figure 2: For convenient comparison the wavelets, all plots are in normalized wiggles. (a) Conventional migration on non-attenuated data. The maximum amplitude of the event before normalization is 0.28; (b) conventional migration on attenuated data. The maximum amplitude of the event before normalization is 0.0015; (c) Q migration on attenuated data. The maximum amplitude of the event before normalization is 0.00011; (d) Q compensation migration on attenuated data. The maximum amplitude of the event before normalization is 0.27.

gular low Q and high Q anomalies, respectively. The $1/Q$ errors are set to 1%, 2%, 4%, 8%, 16%, 32%, and 64% different than the background model.

Ignoring the difference of absolute amplitude scaling, I compare the amplitude spectra between the linearized and the non-linearized image perturbation, by examining the difference of their RMS value ε as follows,

$$\varepsilon\left(\Delta m\right) = \left| \frac{D_{\mathrm{RMS}}\left(\Delta m\right) - d_{\mathrm{RMS}}\left(\Delta m\right)}{D_{\mathrm{RMS}}\left(\Delta m\right)} \right|, \tag{24}$$

where Δm is the perturbation in $1/Q$, $D_{\mathrm{RMS}}\left(\Delta m\right)$ is the RMS value of the normalized amplitude spectrum of the non-linearized image perturbation, and $d_{\mathrm{RMS}}\left(\Delta m\right)$ is the RMS value of the normalized amplitude spectrum of the linearized image perturbation. Figure 3 shows the approximation error ε as Δm increases. The results show that those errors are less than 5%, even for the 64% model error, indicating that WEQTom operator is a good linear approximation.

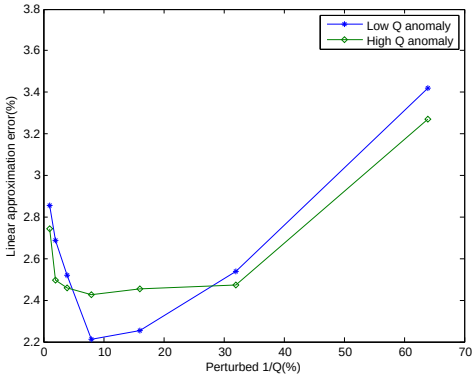

Figure 3: Ignoring the difference of absolute amplitude scaling, I compare the amplitude spectra between the linearized and the non-linearized image perturbation, by examining the difference of their RMS value ε as shown in Equation 24. The $1/Q$ errors are set to 1%, 2%, 4%, 8%, 16%, 32%, and 64% different than the background model. This figure shows the approximation error ε as the model perturbation increases. The results show that those errors are less than 5%, even for the 64% model error, indicating that WEQTom operator is a good linear approximation.

To test the adjoint WEQTom operator $\mathbf{T}^*$, I first run and pass the dot-product test to prove that $\mathbf{T}^*$ is the adjoint of the operator $\mathbf{T}$. Then I test the adjoint operator in a homogeneous background medium with $v = 2000$ m/s and $Q = 50$. The input

of the adjoint tomographic operator is a spike in the image space $\Delta\mathbf{I} = \delta$ ($x = 0$ m, $z = 900$ m). Figure 4(a) and Figure 4(b) show the back-projected Q gradient where the source-receiver offset is 0 km and 1.6 km respectively. Clearly, these back projections have a banana-donut shape and are spread along the wavepaths from the source to the perturbed image point and from the perturbed image point to the receiver.

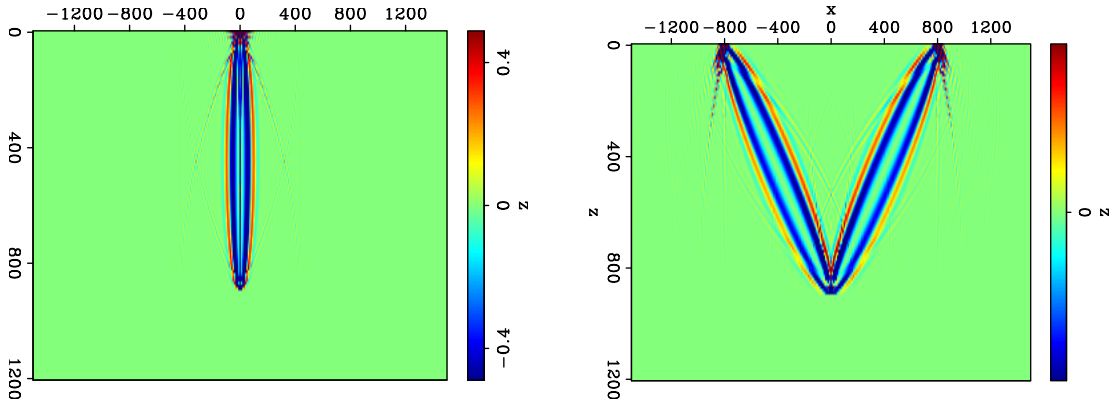

(a) (b)

Figure 4: 2D impulse responses for Q: (a) zero-offset impulse responses; (b) impulse responses when source-receiver offset is 1.6 km.

Preliminary results on 2-D examples

This section applies the WEQTom to two 2-D synthetic examples to update an inaccurate Q model. The first test model has the same geometry and acquisition as the one used in the forward WEQTom operator testing. Again, the background medium is homogeneous with constant velocity (2000 m/s) and constant Q ($Q = 50$). Figure 5(a) and Figure 5(b) show the true Q perturbations, which are 10% lower and higher than the background Q, respectively.

I model the data using the true Q model (the background plus the perturbation), and use the background Q model as the initial model. After compensation migration on the attenuated data with the initial model, the reflectivities (normalized to be 1) are automatically picked from the background image as shown in Figure 6, which serve as the input for the target image.

Figure 7 shows the image perturbation obtained by subtracting the background image from the true image. These images have larger perturbation underneath the Q anomaly than in the area far away from the anomaly. In addition, the sign of the amplitude of the middle lobe of the reflector in Figure 7 indicates the direction for updates. The positive amplitude of the middle lobe of the reflector in Figure 7(a) indicates the background image is undercompensated, and smaller Q is needed for the updates. The reverse is true for Figure 7(b).

In the first iteration, WEQTom back-projects the perturbed image in Figure 7 into the model space, and outputs the gradient for the model perturbation, as shown in Figure 8. Comparing Figure 5 and Figure 8, I can see that the gradients provide the correct direction and shape of the perturbation to conduct a line search in a given inversion scheme. The diverged energy around the anomaly in Figure 8 is caused by the acquisition limitation. Figure 9 shows the inversion results using steepest descent algorithm after 3 iterations. The results show that both the shape and the values of the Q anomalies are recovered.

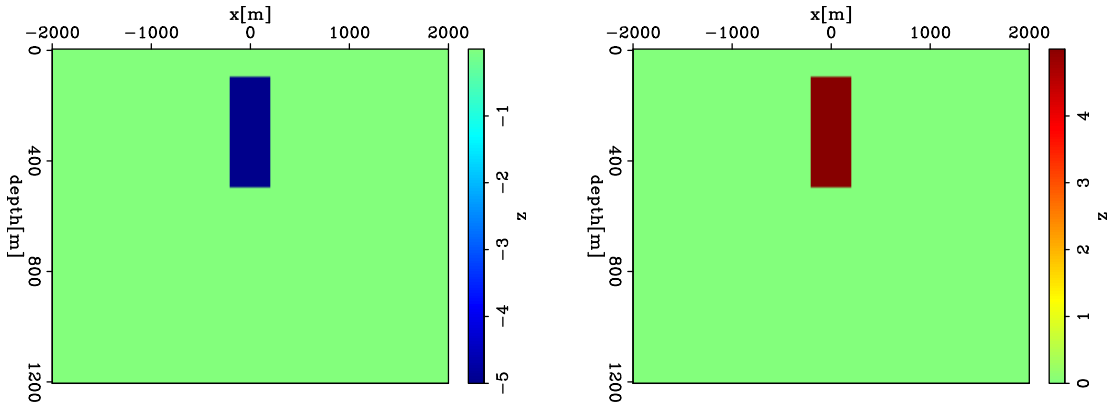

(a) (b)

Figure 5: Q perturbations: (a) rectangular Q anomaly that is 10% lower than the background Q; (b) rectangular Q anomaly that is 10% higher than the background Q.

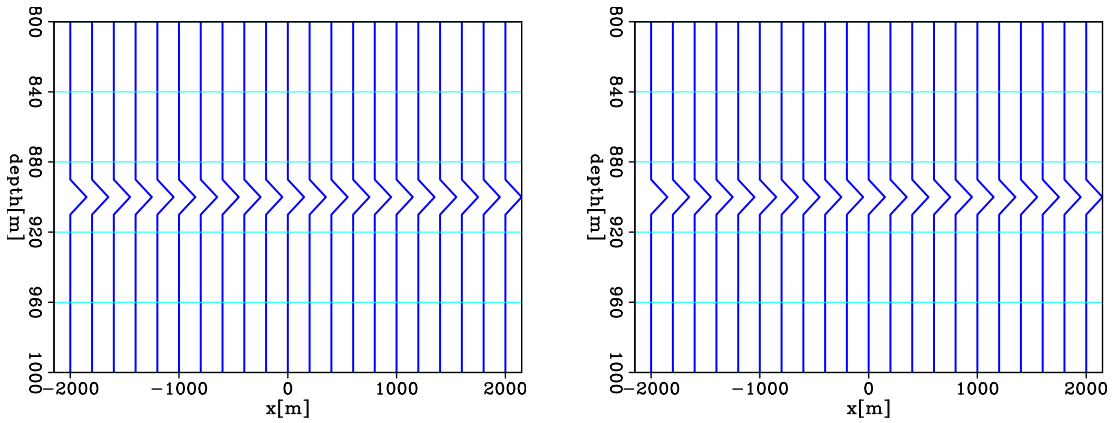

(a) (b)

Figure 6: (a) Picked reflectivities from the background image, migrated from the data with the low-Q anomaly; (b) Picked reflectivities from the background image, migrated from the data with the high-Q anomaly. Reflectivities are normalized to 1.0.

The second test example is modeled on a realistic subsurface structure with an absorptive gas cloud. Figure 10(a) shows the velocity model with multiple reflectors,

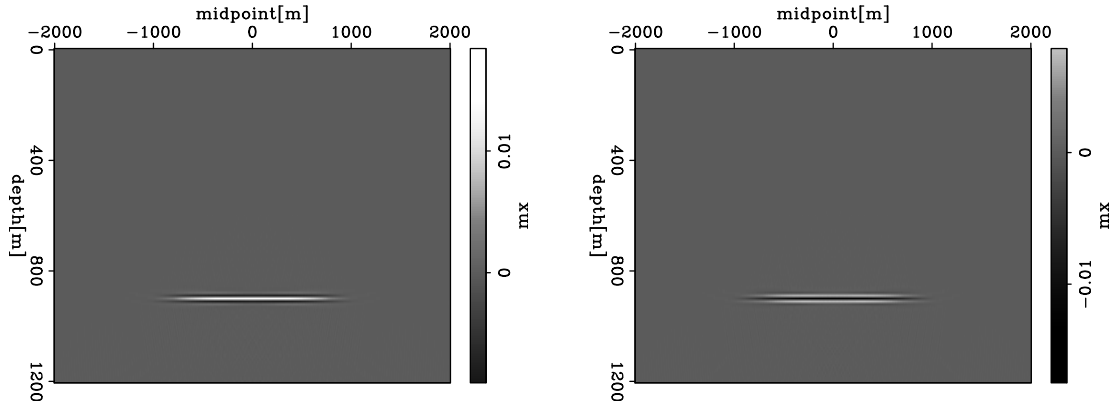

(a) (b)

Figure 7: (a) Image perturbation caused by the perturbed model in Figure 5(a); (b) Image perturbation caused by the perturbed model in Figure 5(b)

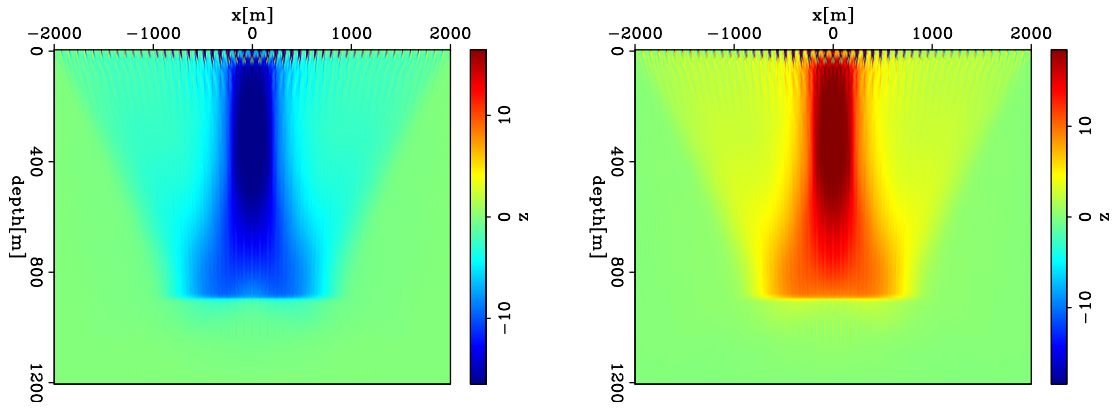

(a) (b)

Figure 8: (a) Back-resolved gradient for the model updates generated from Figure 5(a); (b) Back-resolved gradient for the model updates generated from Figure 5(b);

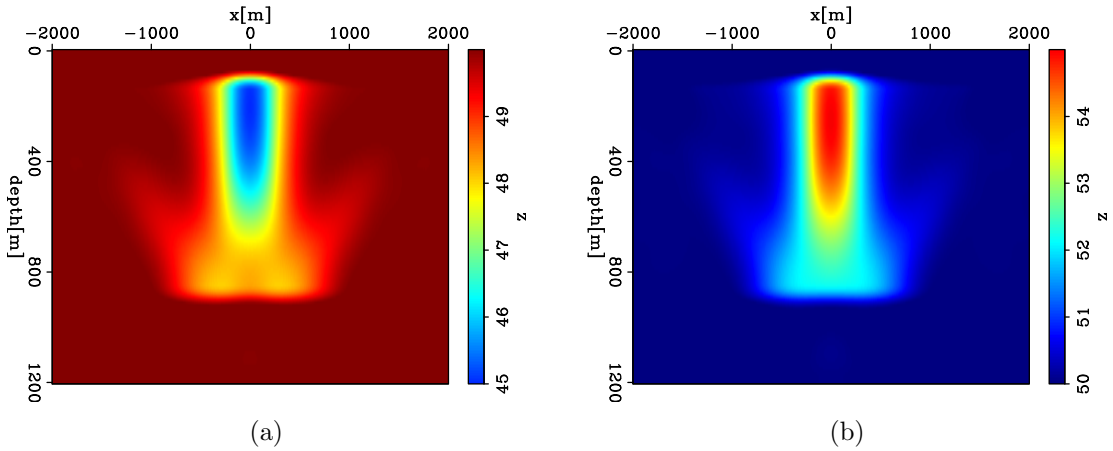

(a) (b)

Figure 9: The inversion results using steepest descent algorithm after 3 iterations: (a) inversion results of the low Q anomaly shown in Figure 5(a); (b) inversion results of the high Q anomaly shown in Figure 5(b).

and Figure 10(b) presents a Gaussian Q anomaly in a non-attenuating medium. The data are modeled with 3 km maximum offset, 10 m receiver spacing, and 40 m source spacing.

I use a non-attenuating medium as the initial model. The normalized reflectivities (shown in Figure 11) for the target image are automatically picked after compensation migration with the initial model. Figure 12(a) shows the image perturbation with strong energy underneath the anomaly, indicating that the reflections below the absorptive cloud are influenced by attenuation the most. Figure 12(b) show the inversion results using steepest descent algorithm after 4 iterations. As the initial model is far from the true model, the low Q anomaly is partially recovered in Figure 12(b), and hence more iterations are needed to better retrieve the true model.

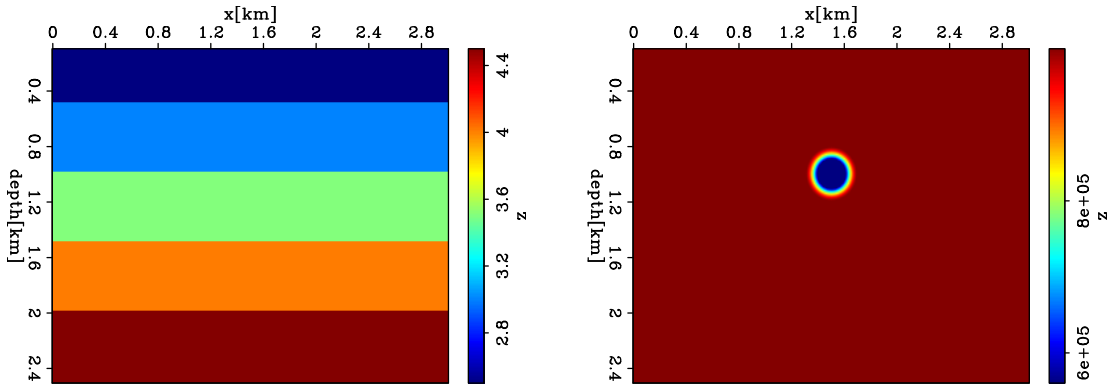

(a) (b)

Figure 10: (a) Velocity model with multiple reflectors; (b) Q model with a Gaussian anomaly in a non-attenuating medium.

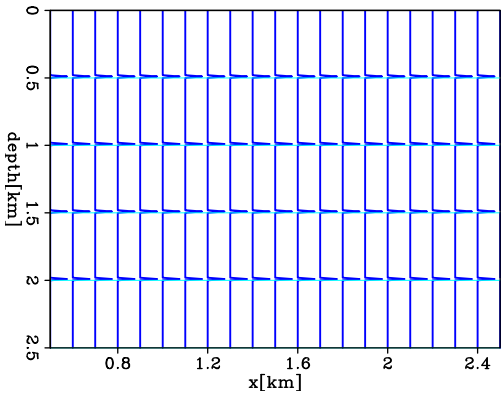

Figure 11: The normalized reflectivities for the target image are automatically picked after compensation migration with the initial model.

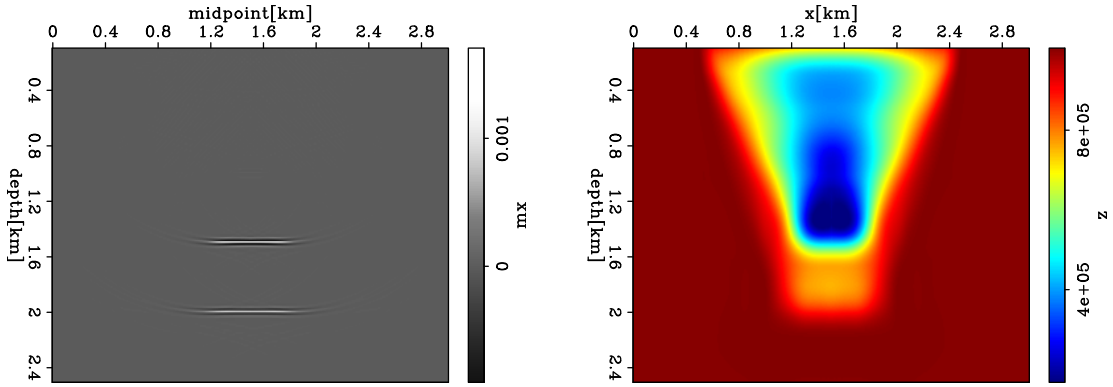

(a) (b)

Figure 12: (a)Image perturbation obtained by subtracting the background image from the true image; (b) Inversion results using steepest descent algorithm after 4 iterations.

FUTURE WORK

- **Investigation of isolating events**

  To estimate the image perturbation, isolating each event is a difficult task for the model with closely spaced reflectors. Errors in isolating each event will introduce spectral interference to degrade the accuracy of model building. Therefore, I will investigate the influence of the event-windowing parameters on the spectra, such as the window length, window overlaps and window tapering, to find the most accurate way of windowing.

- **Better objective function**

  Q back-projection using prestack image gathers

  A method based on prestack image gathers will be tested in the future. I hope to obtain high resolution thanks to the redundant information in the prestack domain.

  Better prestack image gathers

  Besides constructing the common-image gathers with spatial angle at every location in space (ADCIG), Sava and Fomel (2006) introduced an alternative prestack imaging condition in which they preserve multiple lags of the time crosscorrelation. These prestack images are described as functions of time shifts as opposed to space shifts between source and receiver wavefields. Since time shifts can be directly transformed into the temporal frequency domain, I will investigate whether this domain could avoid the spectral stretch and the requirement for preknowledge of opening angles and dipping angles as discussed in the ADCIG method. Furthermore, time-shift imaging is cheaper to apply than space-shift imaging according to Sava and Fomel (2006), and thus it might alleviate some of the difficulties posed by costly cross-correlations in the 3D space-shift imaging condition.

- **Apply Q compensation migration to inversion-based imaging**

  Compensation migration with our estimated Q recovers the energy loss due to attenuation, and hence it may help the inversion-based imaging method -known as least-squares migration (Lambare et al., 1992; Nemeth et al., 1999; Kuhl and Sacchi, 2003), or linearized wavefield inversion (Clapp, 2005; Valenciano et al., 2006; Valenciano, 2008). The code for this inversion is available in the recent SEP report (Wong et al., 2012), and can be implanted with Q compensation migration in the future.

DATA

After synthetic tests, the work described above will be extended to three dimensions on field datasets. There are two kinds of geological environments that I am interested in.

The first setting contains absorptive gas clouds, which is a common phenomenon in the North Sea. The strong absorption of these gas clouds affects the ability to accurately predict/interpret the deeper reservoir properties and structure. I worked on two North Sea datasets with this feature in ConocoPhillips, summer 2012. They are 3D Ekofisk LoFS OBC data, and 2001 3D Eldfisk OBC data. I am requesting the permission to use them for my thesis.

The second setting is karst in the shallow subsurface, which exists in the east part of Gulf of Mexico. Experiments show that when filled with water, karst has strong attenuation effects, and hence greatly degrades the image quality below. Therefore, I'd like to test my algorithm on the karst environment.

RESOURCES AND TIMELINE

Software

Most of the software needed is already available for WEMVA at SEP, and can be used for the image-space WEQTom method. The code for this method is built upon Yaxun's WEMVA code, which has already incorporated OpenMP for computational efficiency. To further lower the computational cost, one possible solution is to extend the tomography program from CPU to GPU using the CUDA programming environment. Besides SEPlib and SEP3D, Madagascar is another source for multi-dimensional data analysis. In addition, I have built up the preliminary tomography scheme for surface seismic data, and I will make corresponding changes when more data become available for my research.

Hardware

The proposed inversion scheme requires application of migration, and forward and adjoint tomography several times in each iteration, and therefore it will take a large amount of computation time.

In addition to current SEP computers, SEP students have access to CEES clusters and hard disks as well. Therefore, the computation resources are more than sufficient for my project.

Timeline

- Ongoing: Work on my inversion scheme. Implement the code for inversion, then test and optimize this code on the synthetic example shown in the previous section before next quarter.

- Winter 2013 -Spring 2013: Work on prestack image gathers. Implement the code for generating the prestacked gather proposed by Sava and Fomel (2006), and use it for the proposed objective function. Compare this domain with ADCIG and stacked image to better understand pros and cons for each method.
- Summer 2013: Internship
- Fall 2013 - Winter 2014: Optimize code, test on 2-D field datasets.
- Spring 2014: Test on 3-D synthetic datasets.
- Summer 2014: Internship
- Fall 2014 - Spring 2015: Test on 3-D field datasets.
- Summer 2015 - Spring 2016: Write thesis.
- Spring 2016: Graduate?

REFERENCES

Best, A. I., C. MaCann, and J. Sothcott, 1994, The relationships between the velocities, attenuations, and petrophysical properties of reservoir sedimentary rocks: Geophysical Prospecting, **42**, 151–178.

Biondi, B. L., 2006, 3-D seismic imaging.

Brzostowski, M. A. and G. A. McMechan, 1992, 3-D tomographic imaging of near-surface seismic velocity and attenuation: Geophysics, **57**, 396–403.

Claerbout, J. F., 1971, Towards a unified theory of reflector mapping: Geophysics, **36**, 467–481.

Clapp, M. L., 2005, Imaging under salt: Illumination compensation by regularized inversion: PhD thesis, Stanford University.

Clark, R. A., P. M. Benson, A. J. Carter, and C. A. G. Moreno, 2009, Anisotropic P-wave attenuation measured from a multi-azimuth surface seismic reflection survey: Geophysical Prospecting, **57**, 835–845.

Clark, R. A., A. J. Carter, P. C. Nevill, and P. M. Benson, 2001, Attenuation measurements from surface seismic data Azimuthal variation and time-lapse case studies: 63rd Conference and Technical Exhibition, EAGE, Extended Abstracts, L–28.

Dasgupta, R. and R. A. Clark, 1998, Estimation of Q from surface seismic reflection data: Geophysics, **63**, 2120–2128.

Futterman, W. I., 1962, Dispersive body waves: Journal of Geophysical Research, **67**, 5279–5291.

Kjartansson, E., 1979, Constant Q wave propagation and attenuation: Journal of Geophysical Research, **84**, 4737–4748.

Kuhl, H. and M. D. Sacchi, 2003, Least-squares wave-equation migration for avp/ava inversion: Geophysics, **68**, 262–273.

Lambare, G., J. Virieux, R. Madariaga, and S. Jin, 1992, Iterative asymptotic inversion in the acoustic approximation: Geophysics, **57**, 1138–1154.

Leaney, W. S., 1999, Walkaway Q inversion: 69th Annual International Meeting, SEG, Expanded Abstracts, 1311–1314.

Leggett, M., N. R. Goulty, and J. E. Kragh, 1992, Study of traveltime and amplitude time-lapse tomography using physical model data: Abstracts of 54th EAEG Meeting,, 248–249.

Macrides, C. G. and E. R. Kanasewich, 1987, Seismic attenuation and Poisson's ratios in oil sands from crosshole measurements: Journal of the Canadian Society of Exploration Geophysicists, **23**, 46–55.

Mateeva, A., 2003, Thin horizontal layering as a stratigraphic filter in absorption estimation and seismic deconvolution: PhD thesis, Colorado School of Mines.

Maultzsch, S., M. Chapman, E. Liu, and X. Y. Li, 2007, Modelling and analysis of attenuation anisotropy in multi-azimuth VSP data from the clair field: Geophysical Prospecting, **55**, 627–642.

Nemeth, T., C. Wu, and G. T. Schuster, 1999, Least-squares migration of incomplete reflection data: Geophysics, **64**, 208–221.

Plessix, R. E., 2006, Estimation of velocity and attenuation coefficient maps from crosswell seismic data: Geophysics, **71**, S235–S240.

Quan, Y. and J. M. Harris, 1997, Seismic attenuation tomography using the frequency shift method: Geophysics, **62**, 895–905.

Reine, C., R. A. Clark, and M. van der Baan, 2012a, Robust prestack Q-determination using surface seismic data: Part 1 Method and synthetic examples: Geophysics, **77**, R45–R56.

———, 2012b, Robust prestack Q-determination using surface seismic data: Part 2 3D case study: Geophysics, **77**, B1–B10.

Rickett, J., 2006, Integrated estimation of interval-attenuation profiles: Geophysics, **71**, A19–A23.

———, 2007, Estimating attenuation and the relative information content of amplitude and phase spectra: Geophysics, **72**, R19–R27.

Sava, P. and B. Biondi, 2004, Wave-equation migration velocity analysis-i: Theory: Geophysical Prospecting, **52**, 593606.

Sava, P. and S. Fomel, 2006, Time-shift imaging condition in seismic migration: Geophysics, **71**, S209–S217.

Tonn, R., 1991, The determination of seismic quality factor Q from VSP data: A comparison of different computational techniques: Geophysical Prospecting, **45**, 87–109.

Valenciano, A. A., 2008, Imaging by wave-equation inversion: PhD thesis, Stanford University.

Valenciano, A. A., B. Biondi, and A. Guitton, 2006, Target-oriented wave-equation inversion: Geophysics, **71**, A35–A38.

Valenciano, A. A., N. Chemingui, D. Whitmore, and S. Brandsberg-Dahl, 2011, Wave equation migration with attenuation and anisotropy compensation: 2011 Annual Meeting, SEG, Expanded Abstracts, 232–236.

Ward, R. W. and M. N. Toksoz, 1971, Causes of regional variation of magnitude: SSA Bull, **61**, 649–670.

Winkler, K. W. and A. Nur, 1982, Seismic attenuation: Effects of pore fluids and

frictional sliding: Geophysics, **47**, 1–15.

Wong, M., B. Biondi, and S. Ronen, 2012, Imaging with multiples using linearized full-wave inversion: SEP-Report, **147**, 249–260.

Zucca, J. J., L. J. Hutchings, and P. W. Kasameyer, 1994, Seismic velocity and attenuation structure of the geysers geothermal field, california: Geothermics, **23**, 111–126.